



# Fabrication of Sub-10-nm Plasmonic Gaps for Ultra-Sensitive Raman Spectroscopy

Arif E. Cetin<sup>1</sup> · Cihan Yilmaz<sup>2</sup> · Betty C. Galarreta<sup>3</sup> · Gizem Yilmaz<sup>2</sup> · Hatice Altug<sup>4</sup> · Ahmed Busnaina<sup>2</sup>

Received: 10 October 2019 / Accepted: 6 February 2020  
© Springer Science+Business Media, LLC, part of Springer Nature 2020

## Abstract

The past two decades have witnessed the explosion of activities in the field of surface enhanced Raman spectroscopy (SERS). SERS platforms employ nano-structures that excite plasmonic modes with large local electromagnetic fields localized within small gap spaces between each constituting feature. Although the research-oriented SERS platforms yield significant signal enhancements to identify even single molecules, practical SERS-based sensors have not been fully introduced yet. The main reason behind this absence is the need for a cost-effective and reliable manufacturing method for controllable fabrication of plasmonic nano-gaps over large areas. In this article, we introduced a novel manufacturing process that enables fast and scalable fabrication of highly uniform sub-10-nm gaps that could yield large SERS signals. In this process, a conventional electroplating technique is used to produce unique nano-mushroom antenna arrays on a conducting substrate, resulting in controllable gap spaces between mushroom heads. By understanding the nature of mushroom shape antenna formation, we demonstrated the control of inter-metallic gaps down to 5 nm. We showed that the manufactured nano-structures yield Raman enhancements more than  $10^8$ . Providing such large SERS signals that are uniform over large areas, our cost-effective fabrication technique could be very critical to realize practical SERS devices.

**Keywords** Plasmonics · Surface enhanced Raman spectroscopy · Nano-fabrication

## Introduction

Surface enhanced Raman spectroscopy (SERS) is a very powerful technique for investigating molecular finger-prints [1]. In this technique, when molecules are adsorbed on rough metal surfaces or nano-textured structures, the weak Raman scattering is dramatically enhanced by orders of magnitude [2–4]. The strong and unique ability of this technique to access weak

molecular bands making it a very vital platform for detecting even single molecules [5, 6]. SERS's power lies on the spacial overlap between the electromagnetic fields associated with surface plasmons and the molecules of interest at the metal surfaces [7]. Realizing nanometer-sized plasmonic gap spaces, local electromagnetic fields could be dramatically enhanced that triggers strong spectroscopy signals [8–12]. Despite its powerful ability of identifying the nature of molecules for research matter, it is still challenging to employ SERS systems as practical sensor platforms. The main drawback in shifting this system from a scientific tool to a commercial biochemical sensor is the need for a low-cost plasmonic chip with large electromagnetic fields uniformly distributed over large areas. For strong SERS signals, focusing propagating or cavity plasmonic modes within a small mode volume, and precisely overlapping this mode volume with molecules of interest are necessary [13]. However, spatially matching the nearfields and the targeted analytes within this small volume has low probability. This negatively effects practical applications as they should provide flexibility to users to perform their tests on any location within their SERS chip. Therefore, practical SERS platforms need chips with plasmonic hot spots uniformly distributed over very large

---

Arif E. Cetin and Cihan Yilmaz contributed equally to this work.

---

✉ Arif E. Cetin  
arifengin.cetin@ibg.edu.tr

- <sup>1</sup> Izmir Biomedicine and Genome Center, 35330 Balcova, Izmir, Turkey
- <sup>2</sup> NSF Nanoscale Science and Engineering Center for High-Rate Nanomanufacturing (CHN), Northeastern University, Boston, MA 02115, USA
- <sup>3</sup> Departamento de Ciencias-Química, Pontificia Universidad Católica del Perú, Avenida Universitaria 1801, Lima 32 Lima, Perú
- <sup>4</sup> Bioengineering Department, Ecole Polytechnique Federale de Lausanne (EPFL), CH-1015 Lausanne, Switzerland

areas. However, fabricating large number of nano-gaps well-distributed over large areas in a controllable manner is still compelling.

Realizing nano-apertures or nano-antennas closely positioned to realize nano-gaps with E-beam lithography and lift-off step could not be a practical solution as it is very time-consuming and expensive to fabricate such plasmonic features over large areas [14–16]. Nano-particle aggregation methods to create antenna islands with nano-gaps in between [17], or incipient wetness impregnation methods to synthesize particles on substrates [18] have been suggested for realizing SERS chips with large area. However, the control of these gap spaces is challenging that dramatically prevents reproducibility. The problem of controllability has been addressed by employing a template that could guide the assembly of nano-particles on the substrate in a controllable manner [19–23]. While some assembly methods mentioned above demonstrated nanoscale gap control over larger areas [24], they do not achieve a long-range periodicity which has the potential for additional field enhancement [25]. Therefore, there is a strong need for a cost-effective and rapid fabrication method that could yield periodic structures with small gap spaces uniformly distributed over large areas.

In this article, we introduced a low-cost and templated assembly based nano-fabrication technique to realize highly dense nano-features over large areas with sub-10 nm gap spaces to create large Raman signal enhancements. Unlike the other templated assembly methods, our technique has the flexibility of arranging the shape and the size of the nano-particles and the gap space between each another, as well as ensures a uniform periodicity over large areas. Our technique employs E-beam lithography and electroplating that could enable uniform periodic antenna islands over a square millimeter area. Possessing these unique advantages, our technique could open doors to realize plasmonic chips composed of large-scale and uniform plasmonic antennas that yield dramatic Raman enhancements, e.g.,  $5 \times 10^8$ , for ultra-sensitive SERS applications.

## Fabrication of Mushroom Shape Antennas

The proposed SERS platform employs periodic gold mushroom shape antennas standing on a gold substrate as shown in Fig. 1. The antennas were fabricated using electroplating by applying a DC voltage between the conducting substrate and the counter electrode through a gold electrolyte solution. First, circular shape periodic vias were created inside of a polymethyl methacrylate (PMMA) resist coated on a gold substrate by E-beam lithography. The gold layer (denoted as conducting substrate in Fig. 1b) under the PMMA film served as a seed layer during the electroplating process. Due to the electrochemical reactions at the metal–electrolyte interface,

the gold atoms nucleated on the seed layer and grew vertically in the vias. The dimensions of the electroplated nano-pillars were controlled by the diameter and the height of the vias. For a constant current density, we used the Faraday's law to determine the electroplating rate (metal height per minute):

$$R = \frac{D \cdot A}{n \cdot F \cdot \rho}$$

where  $R$  is the plating rate (cm/s),  $A$  is the molecular weight of the metal (g/mol),  $n$  is the valence of the dissolved metal in solution (equivalents/mol),  $F$  is Faraday's constant (C/equivalent),  $\rho$  is the density of the metal (g/cm<sup>3</sup>), and  $D$  is the current density (A/cm<sup>2</sup>). We estimated the electroplating rate of gold at a current density of 2.5 mA/cm<sup>2</sup> to be 82 nm/min. Our experiments showed that electroplating of the gold solution produced approximately 150 nm-high nano-pillars in 110 s, verifying the calculated electroplating rate. The height of the nano-pillars can be adjusted by controlling the electroplating time. If plating continues after the vias become completely full (realizing nano-pillars which will be mushroom stalk), gold deposition over the PMMA surface forms mushroom-like nano-structures (due to the formation of the cap-like structures on top of the nano-pillars). Figure 1 a and b show the schematics of two scenarios when the vias are half full and over deposited, respectively. After the gold deposition, the PMMA resist was removed with acetone, revealing the mushroom shape antennas on the gold substrate (Fig. 1c). Figure 1 d shows the scanning electron microscopy (SEM) images of the mushroom shape antennas with stalk diameter  $D_I = \sim 200$  nm, cap diameter  $D_{II} = \sim 600$  nm, stalk height  $H = \sim 150$  nm, and cap height  $D_{III} = \sim 400$  nm.

## Controlling Dimension and Gap Space of Mushroom Shape Antennas

In order to understand the mushroom shape antenna formation, we performed 3D fluid dynamics simulations (COMSOL Multiphysics®) and calculated the electric field distribution within the via geometries. In our experimental setup, intensity and shape of the electric field vary depending on the geometrical parameters such as diameter, height, and via spacing [26]. Figure 2 a shows the color-coded electric field magnitude contours for vias with  $D_I = 100$  nm and  $H = 150$  nm under 2V DC voltage. Here, we observed that electric field magnitude was maximum inside the vias and decreased with distance along the normal direction. The high magnitude of the electric field within the vias is a result of the fringing electric field effect due to the amplification of the electric field within the edges of vias. Here, the electric field magnitude at the center of the vias is higher for larger via spacing ( $W$ ). On the other hand, when the spacing is small, the electric field

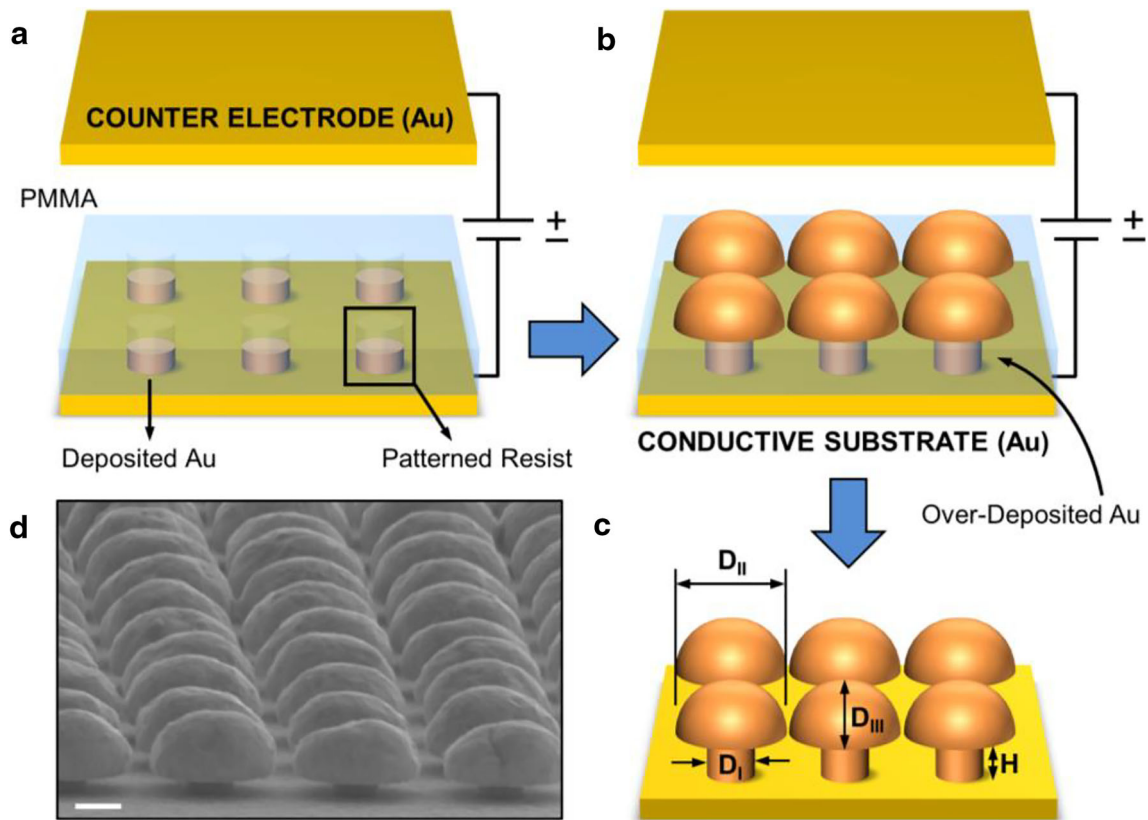


**Fig. 1** Fabrication of mushroom shape antennas. Schematic illustration of the electroplating based fabrication method: **a** vias inside of a PMMA resist were created by E-beam lithography and filled with gold. **b** Over deposited gold resulted in a cap shape layer on top of the PMMA resist. **c**

A simple cleaning step washed away the resist from the surface, revealing the mushroom shape antennas on the conductive substrate. **d** SEM image of the mushroom shape antennas with  $D_I \approx 200$  nm,  $D_{II} \approx 600$  nm,  $D_{III} \approx 400$ , and  $H \approx 150$  nm. Scale: 200  $\mu$ m

contours interact with each other, which results in lower electric field within the vias. More importantly, electric field intensity contours right above the vias are radial. Therefore,

when the electroplating process resumes after the via is completely filled, the metal deposition process follows the electric field intensity distribution that results in mushroom

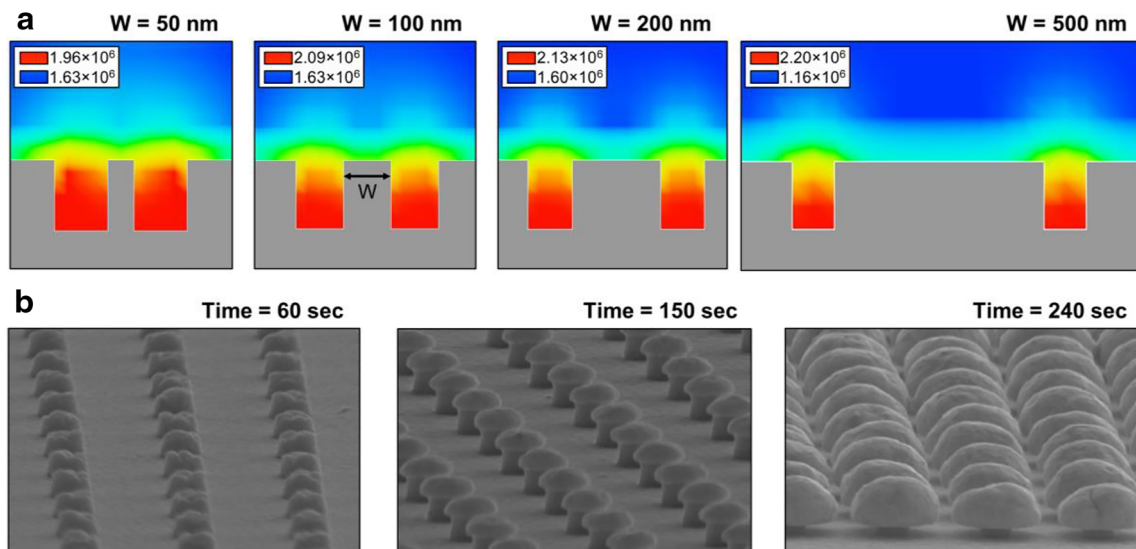


**Fig. 2** Formation and control of mushroom shape antennas. **a** 3D fluid dynamics simulation showing color-coded electric field magnitude contours ( $D_I = 100$  nm,  $H = 150$  nm) for different via spacing ( $W$ ) under an

applied voltage of 2V. **b** SEM images showing the progress of the mushroom shape antenna formation for the via parameters,  $D_I \approx 200$  nm,  $H \approx 150$  nm, and  $W \approx 450$  nm

shape nano-structures. Here, the via spacing is the key to fabricate the mushroom shape antennas. For example, Fig. 2a shows the field intensity distributions for different via spacing at  $D_I = 100$  nm, e.g., for  $W = 50$  and  $100$  nm, the electric field contours above the vias merge, while for  $W = 200$  and  $500$  nm, they are well separated. Smaller via spacing causes an interaction between electric fields of adjacent, i.e., the two adjacent mushroom antennas are expected to merge. This is not favorable for SERS as the enhancement factor would significantly decrease in the absence of a nanometer size gap spaces. Here, we designed our template in such a way that the caps of the mushrooms are not expected to merge even when the metal deposition continues after the vias are completely filled. For our experiments, the distance between two adjacent vias were chosen to be  $450$  nm.

The cap dimensions of the mushroom shape antennas and the gap space between them could be also controlled by the electroplating time. Figure 2 b shows the progress of the mushroom shape antenna formation for the vias with  $D_I = \sim 200$  nm and  $H = \sim 150$  nm. At  $t = 60$  s, the nano-pillars within the vias were almost completed. For the via spacing  $W = \sim 450$  nm, when electroplating was performed at  $t = 150$  s, the diameter of the caps became  $\sim 300$  nm, resulting in  $\sim 400$ -nm gap spaces between mushroom caps. As the electroplating time increases ( $t = 240$  s), the cap of the mushroom shape antennas became larger (e.g.,  $D_{II}$  and  $D_{III}$  increase) and the two antennas got closer to each other, creating much smaller gap spaces.

Based on our experiments, we found at the electroplating time of around  $220$  s, the mushroom caps became very close and the time should be carefully controlled to avoid metals from touching each other. Figure 3 shows the SEM images of the optimized mushroom shape antennas with a  $\sim 800$ -nm cap diameter, where the gap spaces between mushroom caps are less than  $10$  nm. The electroplating time was set to  $230$  s, and the mushroom shape antennas with a uniform array could be fabricated over contiguous areas up to  $50 \mu\text{m} \times 50 \mu\text{m}$  (Fig. 3a). The uniformity of the gap spaces is affected by the cap diameter. Since the shape of the mushroom caps in the

array was not uniform, the gap spaces between adjacent antennas varied between  $5$  and  $50$  nm. For approximately  $90\%$  of the fabrication area, the gap space was less than  $10$  nm (Fig. 3b). Therefore, this high uniformity of the small gap spaces could eliminate the effect of the larger ones on averaging the SERS signal over large areas. Figure 3 c demonstrates the strength of our fabrication method on creating very small features, i.e., the 2 adjacent mushroom shape antennas were separated by only a  $\sim 5$ -nm gap space.

## Optical Characterization of Mushroom Shape Antennas

Figure 4 a shows the experimentally and numerically obtained plasmonic signatures of the mushroom shape antennas, e.g., (green line) backscatter intensity spectrum measured from the assembled antenna areas by dark-field spectroscopy and (black line) electric field intensity spectrum calculated at a single spot within the gap space with finite-difference time-domain (FDTD) simulations. The plasmonic resonance, calculated by the FDTD simulations for a mushroom shape antenna arrays with a  $5$ -nm gap space, was found at  $\sim 735$  nm with a full width half maximum of  $\sim 250$  nm which was in a good agreement with the dark-field spectroscopy result.

In dark-field spectroscopy measurements, samples were illuminated by a dark-field condenser with  $NA = 1.2$ . The signal was collected by an objective lens with  $NA = 0.25$ . Reflection was collected through an Andor SR303i spectrometer with an Andor DU401-BR-DD Charge-Coupled Device (CCD) camera. The background signal obtained from an adjacent gold area was subtracted from the original spectrum and normalized by the profile of the light source. FDTD calculations were performed with Lumerical Inc. FDTD Solutions. In FDTD simulations, dielectric constant of gold was taken from Palik 1985. For the unit cell consisting a single mushroom shape antenna, periodic boundary condition was used along the  $x$ - and  $y$ -directions in order to create collective array behavior, and perfectly matched boundary condition was used

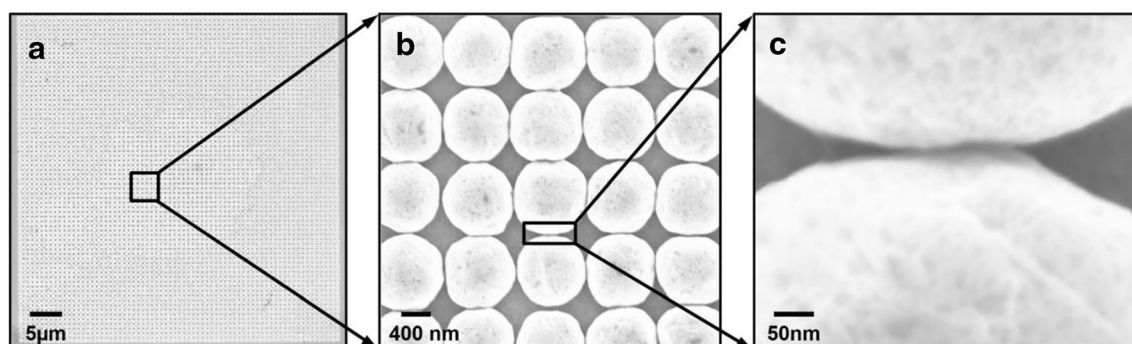


**Fig. 3** Fabrication quality of mushroom shape antennas. SEM images of gold mushroom shape antenna arrays with cap diameter  $\sim 800$  nm. **a** Low-resolution SEM image showing periodic antennas uniform over a

large area. **b** Higher resolution SEM image demonstrating high density of nano-gaps. **c** SEM image showing a gap space as small as  $\sim 5$  nm

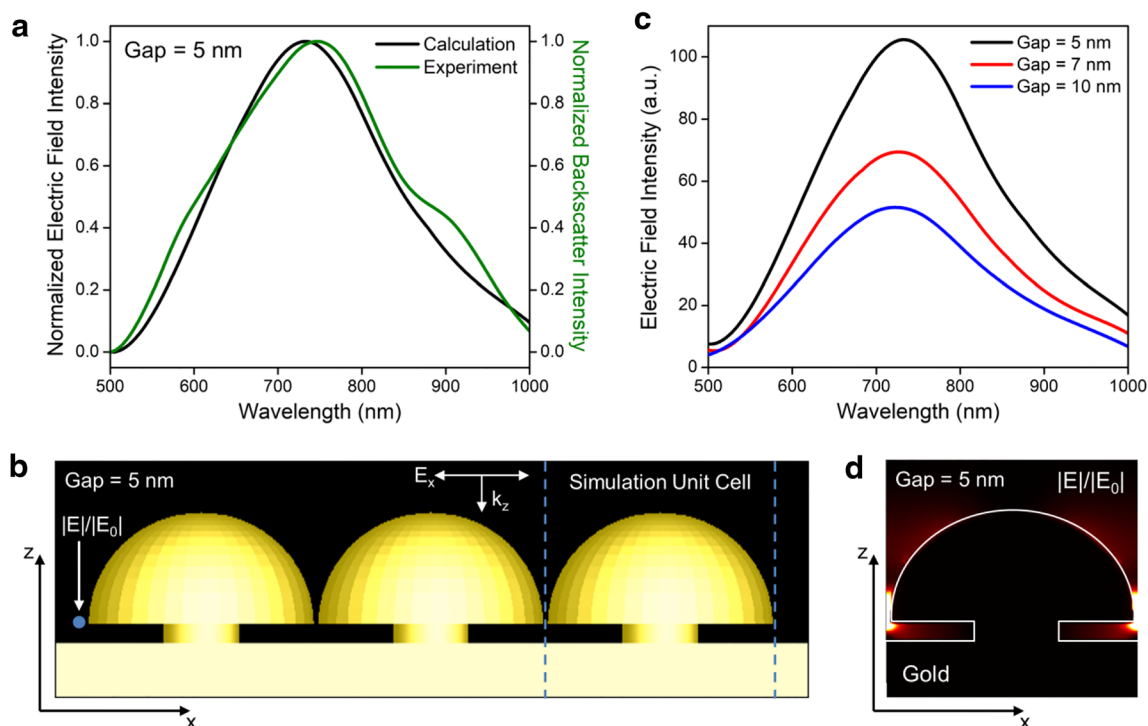


**Fig. 4** Optical properties of mushroom shape antennas. **a** Calculated electric field intensity spectrum (black line) and experimentally measured backscatter intensity spectrum (green line) for mushroom shape antennas. **b** FDTD simulation setup for the nearfield intensity calculations. In the figure, the propagation and the polarization directions of the incident light source were shown. The region denoted with 2 blue-dashed lines is the simulation unit cell (composed of a single

mushroom shape antenna) defined by the boundary conditions mentioned in the text. **c** Electric field intensity spectrum calculated at a single spot (denoted with a blue dot in Fig. 4b) 1 nm away from the mushroom head for different gap spaces (5, 7, and 10 nm). **d** Electric field intensity distribution calculated at the resonance wavelength of the plasmonic mode determined from Fig. 4a

along the illumination direction,  $z$ . Incident light was a plane wave, propagating along the  $z$ -direction and polarized along the  $x$ -axis. In simulations along all directions, mesh size was chosen as 0.5 nm.

The enhancement in Raman signals depends on the frequency, i.e., the frequencies, where both laser excitation and Raman scatter of the targeted chemical bands overlap with the plasmonic mode supported by the antenna geometry, have the strongest SERS signal enhancement [27, 28]. In this paper, we focused on the 785-nm-laser excitation source and the  $1570\text{ cm}^{-1}$  C-C stretch of the benzene ring at 895 nm, both overlapping with the plasmonic mode of the mushroom shape antenna arrays. C-C stretch Raman scatter is well-defined and isolated from other bands, making it a good candidate for Raman analyses.

Figure 4 b shows the unit cell of the simulation region (denoted with 2 blue-dashed lines) that includes a single mushroom shape antenna and the supporting gold substrate. We simulated the electric field enhancement at a single spot 1 nm away from the mushroom head (denoted with a blue dot in Fig. 4b) within the gap space. This spot is the location, where the nearfield intensities are maximum since the plasmonic hot spots are positioned at the antenna edges along the polarization direction [29, 30]. Figure 4 d shows the electric

field intensity distribution (calculated at the resonance wavelength of the plasmonic mode shown in Fig. 4c), demonstrating the strong field localization (namely, hot spot) within the gap space. In Fig. 4c, we calculated the electric field intensity spectrum at the same spot for different gap spaces, demonstrating the fact that electric field intensity within the gap space increases by diminishing gap width. Therefore, our fabrication method, yielding small gap spaces uniformly distributed over large areas, could provide strong Raman signals with small variations within the SERS chip.

## Ultra-Sensitive SERS by Mushroom Shape Antenna

In order to demonstrate the SERS capacity of the mushroom shape antenna system, we calculated the Raman enhancement factor [31] ( $G$ ) per absorbed benzenethiol by comparing the SERS signal from adsorbates on mushroom antennas to the non-enhanced one from the high-density-condensed phase benzenethiol. Raman measurements have been performed with a Kaiser HoloLab 5000R spectrometer of 785-nm excitation. Signals were acquired with a  $\times 50$  (NA = 0.5) and  $\times 100$  (NA = 0.9) objective lenses. The effective beam waists of the

analyzed spots were 6 and 3.5  $\mu\text{m}$  for the  $\times 50$  and  $\times 100$  objective lenses, respectively. The incident power on the samples was between 5 and 15 mW, depending on the Raman signal strength. Acquisition time varied from, e.g., 1 s for mushroom antennas to up to 60 s for the neat benzenethiol.

For the enhancement factor calculation, we used neat benzenethiol, loaded into a sealed cylindrical cell with a 1-mm-path length (Starna Corporation), which was placed onto a Raman microscope stage. Enhancement factor was determined by the following:

$$G = (I_{\text{surf}} \times N_{\text{bulk}}) / (I_{\text{bulk}} \times N_{\text{surf}} \times n^2)$$

where  $I_{\text{surf}}$  and  $I_{\text{bulk}}$  are the peak intensities from the surface-absorbed (on mushroom shape antennas) and liquid benzenethiol, respectively.  $N_{\text{surf}}$  and  $N_{\text{bulk}}$  are the number of molecules on the surface (mushroom shape antennas) and the bulk interrogated (liquid benzenethiol), respectively, and  $n$  is the refractive index of benzenethiol. Here,  $n^2$  was used to consider the difference in the detection angle between liquid and air for the Raman microscope.

The number of molecules on the surface is estimated by the following:

$$N_{\text{bulk}} = \rho \times N_A \times n \times A \times h / M_W$$

where  $\rho$  is the compound density,  $N_A$  is the Avogadro's number,  $A$  is the waist of the interrogating beam,  $h$  is the confocal depth parameter, and  $M_W$  is the molecular weight of the compound [2]. Confocal depth parameter is determined from the depth profiling through focus of a 520- $\text{cm}^{-1}$  peak from a silicon wafer;

$$h = \int_{-\infty}^{+\infty} (I_{520}(z) / I_{520, \text{Max}}) dz$$

which was calculated as 26 and 42  $\mu\text{m}$  for air and benzenethiol (where  $n \approx 1.6$ ), respectively, at  $\times 50$  objective lens. This confocal length is much shorter than the thickness of the liquid cell (1 mm) containing neat benzenethiol compound. For the mushroom shape antennas,  $N_{\text{surf}}$  was estimated from a flat gold surface after the corrections due to the geometry: (i) surface interrogated by the Raman microscope, assumed to be hemispherical as the mushroom cap is hemispherical and (ii) antennas do not cover the full gold surface, i.e., the correction factor is  $2\pi r^2/p^2$ , where  $r = D_{\text{ii}}/2$  and  $p$  is the period of the antenna array. Furthermore, the determination of  $A$  is not necessary as it appears both in the nominator ( $N_{\text{bulk}}$ ) and denominator ( $N_{\text{surf}}$ ) of the equation.

Figure 5 shows the Raman spectra of the benzenethiol-treated mushroom antennas (green line) and the neat liquid benzenethiol (black line), demonstrating their good correlation in peak positions. The high enhancement factors in SERS signals could be achieved in the presence of large local electromagnetic fields right at the sensing surface, allowing

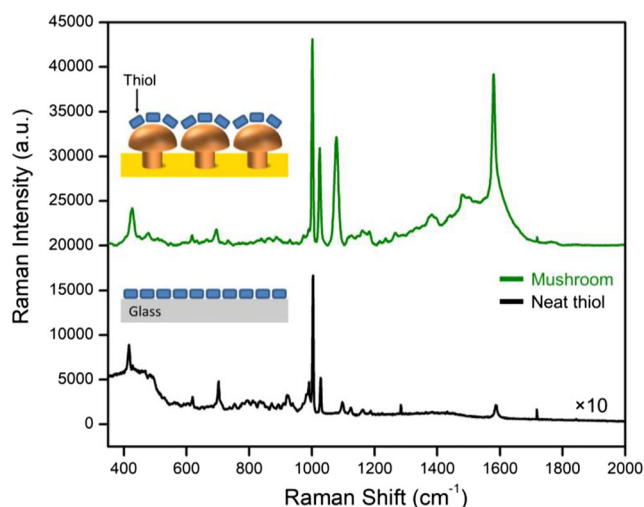


**Fig. 5** SERS properties of mushroom shape antenna. Raman spectra of benzenethiol for neat liquid benzenethiol multiplied by a factor of 10 (black line) and adsorbed benzenethiol on the gold mushroom shape antenna array with sub-10-nm gap spaces (green line) excited with a 785-nm laser

strong light-matter interactions. Hence, the mushroom shape antennas with sub-10-nm gap spaces well-distributed over a large area could provide significant signal enhancements. Using mushroom shape antennas for 1570  $\text{cm}^{-1}$  C-C stretch of benzene ring, we determined,  $G = 5 \times 10^8$ , which is a very advantages enhancement factor for ultra-sensitive SERS applications.

## Conclusions

In conclusion, we introduced a cost-effective, fast, and reliable manufacturing technique for controllable fabrication of nano-features supporting plasmonic hot spots over large areas. Our scalable fabrication method could realize highly uniform sub-10-nm gap spaces with very small variations. We fabricated unique mushroom shape antenna arrays on a conducting substrate, supporting plasmonic resonances with large local electromagnetic fields within the gap spaces, which is very critical for ultra-sensitive SERS applications. Theoretically understanding the nature of mushroom shape antenna formation, we could fabricate inter-metallic gaps down to 5 nm with more than 90% homogeneity over large areas. With such geometry, we could show Raman enhancement as large as  $5 \times 10^8$ . We believe in the future, our technique could serve as a method for manufacturing ultra-sensitive, reliable, and large array SERS devices for practical applications.

**Acknowledgments** A.E.C. acknowledges Izmir Biomedicine and Genome Center Start-Up Research Grant and the BAGEP Award of the Science Academy.

## References

- Blackie EJ, Le Ru EC, Etchegoin PG (2009) Single-molecule surface-enhanced Raman spectroscopy of nonresonant molecules. *J Am Chem Soc* 131:14466–14472. <https://doi.org/10.1021/ja905319w>
- Le Ru EC, Blackie E, Meyer M, Etchegoin PG (2007) Surface enhanced Raman scattering enhancement factors: a comprehensive study. *J Phys Chem C* 111:13794–13803. <https://doi.org/10.1021/jp0687908>
- Jeanmaire DL, VAN Duyne RP (1977) Surface Raman spectroelectrochemistry: Part I. Heterocyclic. *J Electroanal Chem* 84:1. [https://doi.org/10.1016/S0022-0728\(77\)80224-6](https://doi.org/10.1016/S0022-0728(77)80224-6)
- Fleischmann M, Hendra PJ, McQuillan AJ (1974) Raman spectra of pyridine adsorbed at a silver electrode. *Chem Phys Lett* 26:163–166. [https://doi.org/10.1016/0009-2614\(74\)85388-1](https://doi.org/10.1016/0009-2614(74)85388-1)
- Nie S, Emory SR (1994) Probing single molecules and single nanoparticles by SERS. *Science* 266(80):1102–1106. <https://doi.org/10.1126/science.266.5193.1961>
- Chen C, Li Y, Kerman S, Neutens P, Willems K, Cornelissen S, Lagae L, Stakenborg T, van Dorpe P (2018) High spatial resolution nanoslit SERS for single-molecule nucleobase sensing. *Nat Commun* 9:1–9. <https://doi.org/10.1038/s41467-018-04118-7>
- Vo-Dinh T, Vo-Dinh T, Yan F, Stokes DL (2005) Plasmonics-based nanostructures for surface-enhanced Raman scattering bioanalysis. *Protein Nanotechnol* 300:255–284. <https://doi.org/10.1385/1-59259-858-7:255>
- Cetin AEAE, Aksu S, Turkmen M et al (2015) Theoretical and experimental analysis of subwavelength bowtie-shaped antennas. *J Electromagn Waves Appl* 29:1686–1698. <https://doi.org/10.1080/09205071.2015.1051188>
- Kim NH, Hwang W, Baek K, Rohman MR, Kim J, Kim HW, Mun J, Lee SY, Yun G, Murray J, Ha JW, Rho J, Moskovits M, Kim K (2018) Smart SERS hot spots: single molecules can be positioned in a plasmonic nanojunction using host-guest chemistry. *J Am Chem Soc* 140:4705–4711. <https://doi.org/10.1021/jacs.8b01501>
- Chen W, Zhang S, Kang M, Liu W, Ou Z, Li Y, Zhang Y, Guan Z, Xu H (2018) Probing the limits of plasmonic enhancement using a two-dimensional atomic crystal probe. *Light Sci Appl* 7:1–11. <https://doi.org/10.1038/s41377-018-0056-3>
- Zhou X, Deeb C, Kostcheev S et al (2015) Selective functionalization of the nanopop of a plasmonic dimer. *ACS Photonics* 2:121–129. <https://doi.org/10.1021/ph500331c>
- Nam JM, Oh JW, Lee H, Suh YD (2016) Plasmonic nanogap-enhanced Raman scattering with nanoparticles. *Acc Chem Res* 49:2746–2755. <https://doi.org/10.1021/acs.accounts.6b00409>
- Yang Z, Lin K, Meng L et al (2013) Probing the location of hot spots by surface-enhanced Raman spectroscopy: toward uniform substrates. *ACS Nano* 8:528–536. <https://doi.org/10.1021/nn405073h>
- Shi X, Verschueren D, Pud S, Dekker C (2018) Integrating sub-3 nm plasmonic gaps into solid-state nanopores. *Small* 14:1–6. <https://doi.org/10.1002/sml.201703307>
- Djaker N, Hosten R, Devaux E et al (2010) Surface enhanced Raman scattering on a single nanometric aperture. *J Phys Chem C* 114:16250–16256. <https://doi.org/10.1021/jp104971p>
- Galarreta B, Rupar I, Young A, Lagugn -Labarthe F (2011) Mapping hot-spots in hexagonal arrays of metallic nanotriangles. *J Phys Chem C* 115:15318–15323
- Liu J, Chen L, Duan B et al (2016) Engineering aggregation-induced SERS-active porous Au@ZnS multi-yolk-shell structures for visualization of guest species loading. *RSC Adv* 6:38690–38696. <https://doi.org/10.1039/c6ra04432h>
- Budnyk AP, Damin A, Agostini G, Zecchina A (2010) Gold nanoparticle aggregates immobilized on high surface area silica substrate for efficient and clean SERS applications. *J Phys Chem C* 114:3857–3862. <https://doi.org/10.1021/jp9112816>
- Das Gupta T, Martin-Monier L, Yan W, Bris A, Nguyen-Dang T, Page AG, Ho KT, Yesilk y F, Altug H, Qu Y, Sorin F (2019) Self-assembly of nanostructured glass metasurfaces via templated fluid instabilities. *Nat Nanotechnol* 14:320. <https://doi.org/10.1038/s41565-019-0362-9>
- Varghese B, Cheong FC, Sindhu S, Yu T, Lim CT, Valiyaveetil S, Sow CH (2006) Size selective assembly of colloidal particles on a template by directed self-assembly technique. *Langmuir* 22:8248–8252. <https://doi.org/10.1021/la060732q>
- Waters RF, Ohtsu A, Naya M et al (2016) Templated assembly of metal nanoparticle films on polymer substrates. *Appl Phys Lett* 109. <https://doi.org/10.1063/1.4973202>
- Qi H, Hao H, Xingce F et al (2017) Facile design of ultra-thin anodic aluminum oxide membranes for the fabrication of plasmonic nanoarrays. *Nanotechnology* 28:105301. <https://doi.org/10.1088/1361-6528/aa596d>
- Hughes R, Menumerov E, Neretina S (2017) When lithography meets self-assembly: a review of recent advances in the directed assembly of complex metal nanostructures on planar and textured surfaces. Hybrid strategies in nanolithography Engineering metallic nanostructures for plasmonics and nanophot. *Nanotechnology* 28:282002
- Jiwei Q, Yudong L, Ming Y, Qiang W, Zongqiang C, Wudeng W, Wenqiang L, Xuanyi Y, Jingjun X, Qian S (2013) Large-area high-performance SERS substrates with deep controllable sub-10-nm gap structure fabricated by depositing Au film on the cicada wing. *Nanoscale Res Lett* 8:1–6. <https://doi.org/10.1186/1556-276X-8-437>
- Zheng P, Cushing SK, Suri S, Wu N (2015) Tailoring plasmonic properties of gold nanohole arrays for surface-enhanced Raman scattering. *Phys Chem Chem Phys* 17:21211–21219. <https://doi.org/10.1039/c4cp05291a>
- Yilmaz C, Cetin AEAE, Goutzamanidis G, Huang J, Somu S, Altug H, Wei D, Busnaina A (2014) Three-dimensional crystalline and homogeneous metallic nanostructures using directed assembly of nanoparticles. *ACS Nano* 8:4547–4558. <https://doi.org/10.1021/nn500084g>
- Faulds K, Littleford RE, Graham D et al (2004) Comparison of surface-enhanced resonance Raman scattering from unaggregated and aggregated nanoparticles. *Anal Chem* 76:592–598
- Willets KA, Van Duyne RP (2006) Localized surface plasmon resonance spectroscopy and sensing. *Annu Rev Phys Chem* 58:267–297. <https://doi.org/10.1146/annurev.physchem.58.032806.104607>
- Cetin AEAEAE, Etezadi D, Altug H (2014) Accessible nearfields by nanoantennas on nanopedestals for ultrasensitive vibrational spectroscopy. *Adv Opt Mater* 2:866–872. <https://doi.org/10.1002/adom.201400171>
- Cetin AEAEAE, Coskun AFAF, Galarreta BCBCBC et al (2014) Handheld high-throughput plasmonic biosensor using computational on-chip imaging. *Light Sci Appl* 3. <https://doi.org/10.1038/lsa.2014.3>
- Liberman V, Yilmaz C, Bloomstein TM et al (2010) A nanoparticle convective directed assembly process for the fabrication of periodic surface enhanced Raman spectroscopy substrates. *Adv Mater* 22:4298–4302. <https://doi.org/10.1002/adma.201001670>